POST–ASYMPTOTIC GIANT BRANCH EVOLUTION IN THE LARGE MAGELLANIC CLOUD: A STUDY OF THE CENTRAL STARS OF PLANETARY NEBULAE[1]

Eva Villaver and Letizia Stanghellini[2]

Space Telescope Science Institute, 3700 San Martin Drive, Baltimore, MD 21218;
villaver@stsci.edu, lstanghe@stsci.edu

and

Richard A. Shaw

National Optical Astronomy Observatory, 950 North Cherry Avenue, Tucson, AZ 85719;
shaw@noao.edu

ABSTRACT

We present medium- and broadband *Hubble Space Telescope* (*HST*) photometry of a sample of 35 central stars (CSs) of planetary nebulae (PNs) in the Large Magellanic Cloud (LMC). The observations were made with the Wide Field Planetary Camera 2 (WFPC2) and Space Telescope Imaging Spectrograph instruments on board the *HST*. By observing LMC objects, our sample is free of the distance uncertainty that is the dominant source of error in the determination of CS luminosities in Galactic PNs. By observing with the *HST* we resolve the nebula, and therefore we often detect the CSs unambiguously. We obtain core masses of 16 of the objects by comparing their positions on the H-R diagram with theoretical evolutionary tracks, once we determine the stellar effective temperature through Zanstra analysis. This sample of CS masses is the largest and most reliable set obtained in an extragalactic environment. We find an average mass of 0.65 $M_\odot$, although a few of the objects have very high mass. This average value is consistent with the average mass of the white dwarf population in the Galaxy. As the immediate precursors of white dwarfs, the study of the mass distribution of PN CSs should help to constrain the initial-to-final mass relation within environments of differing metallicity. Finally, by exploring the physical connections between the star and the nebula, we establish the importance of the study of PNs in the LMC to constrain the energy input from the wind during the post–asymptotic giant branch phase.

Subject heading: Magellanic Clouds — planetary nebulae: general — stars: AGB and post-AGB — stars: evolution — stars: fundamental parameters

1. INTRODUCTION

Central stars of planetary nebulae (CSPNs) are the result of the evolution of stars in the approximate mass range 1–8 $M_\odot$ that ascend the asymptotic giant branch (AGB) after hydrogen has been exhausted and helium has been ignited in the core. During the AGB phase, low- and intermediate-mass stars experience high mass-loss rates that remove most of the stellar envelope, leaving behind a stellar core that later on will ionize the previously ejected envelope. The star then enters its evolution in the PN domain. During the PN phase the CS evolves at constant luminosity toward higher effective temperatures, and later descends a white dwarf cooling track after the nuclear energy sources have been exhausted.

The upper initial mass limit for white dwarf production, according to stellar evolution theory, depends on the treatment of two poorly understood mechanisms: mass loss and convection (Blöcker 1995; Herwig 2000); therefore, an observational determination of the initial-to-final mass relation, and therefore the minimum mass of Type II supernova progenitors, depends strongly on the measurements of white dwarf masses.

White dwarfs are observed to posses a very narrow mass distribution, which peaks at ∼0.57 $M_\odot$ and has a tail extending toward larger masses (Bergeron, Saffer, & Liebert 1992; Finley, Koester, & Basri 1997). The CSPNs in the Galaxy are found to peak around the same mass value (Stanghellini et al. 2002b). However, the initial-to-final mass relation is expected to change slightly with the metallicity (Weidemann 1987), and because of the lower metallicity the upper mass limit of white dwarf progenitors is expected to be smaller in the Large Magellanic Cloud (LMC; Umeda et al. 1999; Dominguez et al. 1999; Girardi et al. 2000). The mass distribution of CSPNs in the LMC should reflect this fact, as they are the immediate progenitors of the white dwarf population. Only four masses of CSPNs in the LMC have been determined from direct measurement of the stellar flux (Dopita et al. 1993; Bianchi, Vassiliadis, & Dopita 1997). The mass range of three of these CSs agrees with the range of values found in the Galaxy, and the fourth one has a high-mass progenitor; thus, more mass determinations of CSPNs in the LMC are needed to address the scientific problems described here.

The determination of accurate masses of CSPNs is also important to solve a long-standing problem in PN formation: the likelihood that the mass of the progenitor star determines the morphology of the PN it hosts. Understanding the development of the simplest variety of shapes, from round to

---

bipolar, displayed by PNs is one of the most exciting challenges of the late stellar evolution studies. On the one hand, there is a large amount of observational evidence that shows fundamental differences in the physical and chemical properties between morphological classes. On the other hand, there is still a wide debate about which of the proposed collimation mechanisms operates in PNs, although numerical models are able to reproduce the overall morphologies. While it seems clear that the mechanism is related to the stellar progenitor, it is to be determined whether the mass of the progenitor, its magnetic field (Pascoli 1992; García-Segura et al. 1999), its rotation (Calvet & Peimbert 1983; García-Segura et al. 1999), the presence of a companion star (Livio & Soker 1988), or a substellar object (Livio & Soker 2002) plays the dominant role.

The importance of the progenitor mass in the development of the PN morphology first suggested by Greig (1971) has been corroborated from the N and O chemical enrichment found in the bipolar and extremely axisymmetric morphological classes (Peimbert 1978; Torres-Peimbert & Peimbert 1997). Bipolar PNs in the Galaxy are also found at a lower average distance from the Galactic plane than other morphological classes (Corradi & Schwarz 1995; Manchado et al. 2000; Stanghellini et al. 2002b), suggesting that they evolve from more massive progenitors. The correlations between the CS mass and the morphology for Galactic PN samples has been explored by several authors (Stanghellini, Corradi, & Schwarz 1993; Amnuel 1995; Corradi & Schwarz 1995; Gorny, Stasinska, & Tylenda 1997; Stanghellini et al. 2002b), who have found slightly different mass distributions for the CSs of symmetric and axisymmetric PNs. However, determining CS masses for a statistically significant sample in the Galaxy is not an easy task. Typically, the evolutionary tracks of the CSs of different masses in the H-R diagram show very little variance with the CS luminosity, and since distances to Galactic PNs are very uncertain, so is the estimation of their luminosities. Moreover, CSPNs are faint, and the nebular continuum emission can completely mask the CS.

Hubble Space Telescope (*HST*) offers a unique opportunity to study the CSPNs in the Magellanic Clouds and to explore correlations with PN morphology and with PN physical conditions, with unprecedented accuracy, largely because their distances are independently known. In this paper we determine accurate masses of CSPNs for the largest sample of extragalactic PNs ever studied, and we explore the connections among the fundamental properties of the stars (luminosity, temperature, and mass) and the physical properties of the host nebulae.

We present photometry of 35 CSPNs in the LMC obtained from the Cycle 8 *HST* snapshot survey of LMC PNs by using broadband imaging with the Space Telescope Imaging Spectrograph (STIS), and from the Cycle 9 *HST* medium-band F547M (Strömgren *y*) images obtained with Wide Field Planetary Camera 2 (WFPC2). The broadband images of the 29 PNs observed with STIS have been already published by Shaw et al. (2001, hereafter Paper I), and the line intensities and nebular physical conditions obtained by using *HST* STIS slitless spectroscopy by Stanghellini et al. (2002a, hereafter Paper II). In § 2 and § 3 we describe the observations and the photometric calibration. The CS temperature and luminosity determinations and their distributions versus different nebular parameters are presented in

§ 4. The results are presented in § 5 and discussed and summarized in § 6.

2. OBSERVATIONS

2.1. *STIS Broadband Data*

The STIS observations of 29 of the targets presented in this paper are from the *HST* GO program 8271. The observation log, observing configuration, target selection, acquisition, and a description of the basic calibration (through flat-fielding) can be found in Paper I. The photometry of the CSs was measured from the STIS clear aperture mode images (50CCD). The 50CCD is an unvigneted aperture with a field of view of $52'' \times 52''$ and a focal plane scale of $0\rlap{.}''0507$ pixel^{-1}. In this setting no filter is used, and the shape of the bandpass is governed by the detector (which has a sensitivity from $\sim$2000 to 10300 Å) and by the reflectivity of the optics. The central wavelength of the 50CCD is 5850 Å, and the bandpass is 4410 Å. The FWHM of a point-spread function (PSF) is close to 2 pixels at 5000 Å, and the 90% encircled energy radius is 3 pixels (Leitherer et al. 2001). The observations were made with the CCD detector by using a gain of 1 e^- per analog-to-digital converter unit (ADU). All the exposures were split into two equal components to facilitate cosmic-ray rejection.

Table 1 gives in column (1) the object name, in column (2) the instrument and configuration used for the observation, in column (3) the total integration time, and in column (4) whether or not the CS was detected in the images.

2.2. *WFPC2 F547M Data*

We obtained images of 13 PNs with the WFPC2 instrument on *HST* between April 2000 and May 2001. The WFPC2 observations were executed in GO program 8702, which aimed to recover CSs that were undetected in program 8271, because of severe contamination from nebular continuum, and in GO program 6407 (PI: M. A. Dopita), where only narrowband images were available. Of the 13 targets observed in program 8702, seven are in common with program 8271, and the other six objects are from program 6407.

Two exposures were taken for each of two closely spaced (dithered) pointings, with the object centered on the PC reference aperture. The spatial scale is $0\rlap{.}''0455$ pixel^{-1}. The observations were taken with the filter F547M at a gain of 7 e^- ADU^{-1}. The medium-band F547M (Strömgren *y*) filter (centered at 5454 Å with a bandpass of 487 Å) is a close match to the Johnson *V* filter, although the bandpass is narrow enough to exclude the strongest nebular emission lines ([O III] $\lambda\lambda$4959, 5007; Hα λ6563; and [N II] $\lambda\lambda$6548, 6583). However, nebular continuum emission is present in our images that originates mainly from the recombination of hydrogen. In addition, F547M includes some contribution from weak emission lines such as He I λ5876, He II λ5411, and [Cl III] λ5527. Another possible source of nebular contamination is the " leakage' of the [O III] λ5007 emission into the F547M filter pointed out by Rubin et al. (2002). The radial velocities of the LMC PNs we observed are between 220 and 285 km s^{-1} (Meatheringham et al. 1988a). The central wavelength for these objects will be displaced toward the red by about 4–5 Å. This effect will increase the filter transmission in the [O III] 5007 Å line, which is usually one of the brightest in PNs, by about 0.4%. So for our data,

Name (1)	Instrument and Configuration (2)	Integration (s) (3)	CS Detection (4)
J 41	STIS 50CCD	300	Yes
SMP 4	STIS 50CCD	120	Yes
SMP 9	STIS 50CCD	120	No
	WFPC2 F547M	1600	No
SMP 10	STIS 50CCD	120	Yes
SMP 13	STIS 50CCD	120	Yes
SMP 16	STIS 50CCD	300	No
	WFPC2 F547M	1600	No
SMP 18	STIS 50CCD	120	Yes
SMP 19	STIS 50CCD	120	Yes
	WFPC2 F547M	1600	No
SMP 25	STIS 50CCD	120	Yes
SMP 27	STIS 50CCD	120	Yes
SMP 28	STIS 50CCD	120	Yes
SMP 30	STIS 50CCD	120	Yes
	WFPC2 F547M	1600	No
SMP 31	STIS 50CCD	120	Yes
SMP 33	WFPC2 F547M	1600	No
SMP 34	STIS 50CCD	120	Yes
SMP 42	WFPC2 F547M	1600	Yes
SMP 46	STIS 50CCD	120	No
	WFPC2 F547M	1600	No
SMP 50	WFPC2 F547M	1600	Yes
SMP 52	WFPC2 F547M	1600	Yes
SMP 53	STIS 50CCD	120	No
	WFPC2 F547M	800	No
SMP 56	WFPC2 F547M	1600	Yes
SMP 58	STIS 50CCD	120	Yes
SMP 59	STIS 50CCD	120	Yes
SMP 63	WFPC2 F547M	800	Yes
SMP 65	STIS 50CCD	120	Yes
SMP 71	STIS 50CCD	120	No
SMP 78	STIS 50CCD	120	No
	WFPC2 F547M	800	No
SMP 79	STIS 50CCD	120	No
SMP 80	STIS 50CCD	120	Yes
SMP 81	STIS 50CCD	120	Yes
SMP 93	STIS 50CCD	120	No
SMP 94	STIS 50CCD	120	Yes
SMP 95	STIS 50CCD	120	No
SMP 100	STIS 50CCD	120	Yes
SMP 102	STIS 50CCD	120	Yes

some emission from the [O III] 5007 Å line in the F547M filter is very likely.

The images were calibrated using the standard *HST* data pipeline (see Baggett et al. 2002). Duplicate exposures were combined, but with rejection of cosmic rays. Further rejection of cosmic rays and hot pixels was applied when the dithered images were aligned and co-added.

3. ANALYSIS

3.1. *Photometric Technique*

The application of conventional photometric methods to CSPNs in the Magellanic Clouds is currently possible only with the spatial resolution offered by *HST*, when the nebula is resolved and the separate nebular and stellar contribu-

tions to the emission can be distinguished. We have applied aperture photometry techniques to our data by using the IRAF[3] PHOT task. Briefly, we measured the flux within a circular aperture centered on the star. The flux within this aperture also includes the nebular emission projected onto the star, for which we correct by subtracting the nebular flux in an annulus surrounding the aperture of the star. The nebular emission may be very inhomogeneous, so for each object we evaluated the radial distribution of nebular flux to select the optimal aperture width and position.

The stellar aperture was chosen to have a radius of 2 and 3 pixels for the STIS and the WFPC2 images, respectively. Bigger apertures increase the noise without increasing the signal, and a smaller aperture is not advisable since the enclosed flux will depend on the position of the star within the pixel. The fraction of the stellar PSF that falls outside the stellar aperture is taken into account with an aperture correction that is well determined from the instrument PSFs.

For most of the objects in our sample, the contribution of the nebula can be accurately subtracted by using the median of the flux in an annulus with a width of 2 pixels adjacent to the stellar aperture. Strong variations around the median of the subtracted nebular flux are reflected in the standard deviation and, therefore, are propagated into the errors of the measured magnitudes. In those cases in which the nebular emission decreases very sharply with the radius (e.g., for very compact PNs) or when the CS emission is faint compared with the nebula, an accurate value of the nebular flux for subtraction could not be determined with this technique without very large errors in the photometry. In those cases we performed the photometry on an image from which the two-dimensional nebular emission had been removed. We constructed a nebular emission image for this purpose by co-adding the available monochromatic images taken from the STIS spectroscopy (see Paper II), where the individual monochromatic images were weighted by the throughput of the 50CCD bandpass for that wavelength. We considered the Hβ; [O III] $\lambda4959$, 5007; Hα; and [N II] $\lambda6548$, 6584 contribution. We subtracted the resulting nebular image from the 50CCD image. We then used our annulus subtraction technique to eliminate any residual nebular contribution.

To test the validity of the procedure we have applied the two methods described above to four randomly selected PNs (SMP 4, SMP 10, SMP 27, and SMP 80), that is, aperture photometry on a nebular subtracted image and aperture photometry when the nebula has not been previously subtracted. In both cases the emission of the nebula, or the residuals from the nebular subtraction, are determined in an annulus surrounding the stellar aperture. The differences in the magnitudes measured in the cases in which we tested both methods are at the 0.001 mag level, which is smaller than the errors in the magnitudes. We believe that for most of the objects it is not necessary to subtract a nebular image before performing the aperture photometry. But in those cases for which either the CS is detected at a very low level above the nebular emission or the nebula is very

compact, we were able to reduce the errors greatly by subtracting the nebula prior to performing the photometry.

When the CS is not detected (i.e., no stellar PSF appears above the nebular level), we computed a lower limit to the CS magnitude by measuring the flux inside a stellar aperture at the geometric center of the nebula (i.e., the most likely position of the CS). The nebular background flux was measured in an adjacent aperture and then subtracted. The lower limit to the stellar magnitude is the measured magnitude minus the error in magnitudes. Obviously, the lower limits for the magnitude are very uncertain since they depend on the flux measured within an aperture that may or may not actually contain the CS. Moreover, it is very difficult to set the nebular level when the CS is not visible, since it depends strongly on a very uncertain position, which could contain the CS.

3.2. Photometric Calibration
3.2.1. STIS Broadband Data

We have transformed our net instrumental count rate to magnitudes measured in the STMAG[4] system by using the zero-point calibration given by Brown et al. (2002). (The zero point used was 26.518.) The STIS charge transfer efficiency (CTE) has been characterized by Gilliland, Goudfrooij, & Kimble (1999), and the effect on the magnitudes has been shown to be below 0.01 mag (Rejkuba et al. 2000), except for very faint stars on the edge of the CCD, which was never our case; therefore, we have ignored the CTE correction for the STIS data since it is negligible for our purposes. In this observing mode, the image distortions can be neglected as well, since they are less than a pixel across the whole detector. The aperture correction applied to the magnitudes measured in a radial aperture of 2 pixels is 0.517 dex, on the basis of the curve of encircled energy derived by Brown et al. (2002) for stars near the field center.

3.2.2. WFPC2 F547M Data

The zero-point calibration to the STMAG system for the filter and observation configuration of the data taken with the WFPC2 was taken from Dolphin (2000a; we used a zero point of 21.544). We have applied the CTE, geometric distortion, and aperture corrections to this data. The CTE correction, which depends on the position on the chip, target brightness, background, date, and observing mode, was determined for our data following the prescriptions of Dolphin (2000a). The geometric distortion in the WFPC2 field, which is removed during calibration during flat-fielding, causes pixels to have different effective areas as a function of position. It does not affect surface photometry, but it affects point-source photometry; therefore, we have applied a correction for geometric distortion depending on the position of the star on the CCD by using a geometric correction image. We have determined the offset between our aperture (3 pixels) and the nominal aperture used for the calibration (0″5 in radius, which correspond to 11 pixels for the PC camera) by selecting isolated bright stars on each field and averaging the difference between the 3 and 11 pixel apertures. Usually, we have averaged the values for five stars on each field. No contaminant correction was applied

---

[4] The STMAG is the Space Telescope magnitude system, based on a spectrum with constant flux per unit wavelength.

since it is significant only for UV observations. To check the calibration of our STMAG instrumental magnitudes we performed PSF photometry on each field with the HSTphot package (Dolphin 2000b). Then we verified that the magnitudes of selected stars on the field measured with HSTphot agreed with our aperture photometry measurements after all the corrections were performed.

3.3. Extinction Correction

To derive the stellar extinction correction we used the nebular Balmer decrement. We adopted from Paper II the extinction constants for all objects except for SMP 50, SMP 52, SMP 56, and SMP 63 (which were taken from Meatheringham & Dopita 1991a), and SMP 33 and SMP 42 (taken from Meatheringham & Dopita 1991b). The conversion from the nebular extinction constant, c (the logarithm of the total extinction at Hβ), to the color excess, $E(B-V)$, requires some caution (Kaler & Lutz 1985). The approximate relationship between c and $E(B-V)$ depends on the spectral energy distribution (SED) of the target in question. We have used the approximate relation $c = 1.41E(B-V)$. Kaler & Lutz (1985) found that the ratio of c to $E(B-V)$ shows little variation with the stellar temperature but increases with the amount of extinction. Since the amount of extinction measured in our objects is typically small, we are confident about the assumption of a constant value for the relation between c and $E(B-V)$. Adopting a different relation is meaningful only in the cases in which $c \geq 0.2$, which leads to $E(B-V)$ values that change in the second decimal place (i.e., of the order of our photometric errors).

The reliability of our method to determine the stellar extinction assumes that the extinction does not vary across the nebula because of internal absorption by dust. In Paper II no significant variations of the Hβ/Hα ratio were found for heavily reddened objects on spatial scales of ∼0.04 pc, which gives us confidence in the use of c to derive the amount of stellar extinction.

In the wavelength range under consideration, the LMC extinction law is very similar to the Galactic extinction law (Howarth 1983); thus, to convert $E(B-V)$ to total absorption in the V band, we used the interstellar extinction law of Savage & Mathis (1979) and assumed that $R_V = 3.1$. The extinction in magnitudes (A_V) is then $A_V = 2.2c$.

3.4. Transformation to Standard V Magnitudes

The filters in *HST* instruments do not match perfectly the bandpasses of standard photometric systems, such as Johnson-Cousins *UBVRI*, so the transformation from instrumental magnitudes to a standard system depends on the SED of the object observed. For the WFPC2 data the transformation is straightforward because the F547M filter is a close match to the Johnson *V* filter (see Biretta et al. 2002). Our WFPC2 F547M magnitudes have been transformed to the standard *V* magnitudes following the prescriptions of Holtzman et al. (1995). The color $(V-I)$ needed to apply the transformation has been derived via synthetic photometry with IRAF STSDAS SYNPHOT by using a blackbody spectrum to represent the SED of the CSs. The color dependence with temperature and reddening has been determined using as input a range of blackbody temperatures and $E(B-V)$ in the parameter range of our CSPNs. For our purposes, it seems that a blackbody is as good an approximation as any model atmosphere to

represent the SED of CSPNs (Gabler, Kudritzki, & Mendez 1991). We find that the transformation from WFPC2 F547M to standard V magnitudes is rather insensitive to changes in the stellar temperature and reddening within the range of values of our sources. The median of the transformation obtained by using a $(V-I)$ color range derived for CS effective temperatures[5] between 30,000 and 300,000 K is -0.013 mag, with a standard deviation of $\sigma = 0.002$. By using a CS effective temperature of 50,000 K and allowing $E(B-V)$ to change between 0.1 and 1, we obtain a transformation with a median of 0.001 mag and a σ of 0.004. We have converted the WFPC2 magnitudes to standard V by using the median of the transformation obtained for effective temperatures between 30,000 and 300,000 K. We have estimated the error of the transformation to be the quadratic sum of the σ obtained for the range of effective temperatures and the σ obtained for the $E(B-V)$ range considered.

The STIS 50CCD bandpass is very broad, and its response curve is far from that of the standard V filter. Moreover, the transformation from 50CCD to V magnitudes has not been published; therefore, obtaining standard V magnitudes from our 50CCD data requires considerable care. As a first step we used the SYNPHOT package in STSDAS to explore the dependence of the transformation with both the $E(B-V)$ and the CS temperature. We explored the CS temperature range 30,000–300,000 K, and the $E(B-V)$ in the range of our data. We find that the correction is strongly dependent on the extinction and, to a lesser extent, on the temperature of the star; therefore, we have determined the transformations of the 50CCD to V individually for each object by determining the median of the $V-$50CCD colors for blackbodies between 30,000 and 300,000 K and using the $E(B-V)$ value of each source. The σ of the transformation for each object (given for the correction in the range of temperatures) has been added to the error of the magnitude. The highest standard deviation we get is 0.05 mag, and the highest value of the correction is 0.308 mag [for J41, SMP 59, SMP 93, and SMP 102 with $E(B-V) = 0$], although most of the corrections are near 0.1 mag.

In Table 2, we give the results of the photometry. Column (1) gives the PN name (according to the SMP nomenclature when available); column (2) gives the V magnitude or its lower limit, as well as the associated errors. The error value includes the random error (photon noise and read noise), systematic error (CS flux and sky), and the errors in the calibration. In those cases for which the data were saturated we note that circumstance in the table with the measurement of the magnitude. The magnitudes derived from saturated data have not been used for the analysis in the rest of the paper. Unless noted otherwise the magnitudes obtained from the STIS data are given. The color excesses used to correct for extinction are listed in column (3).

4. DETERMINATION OF THE CS EFFECTIVE TEMPERATURE

The temperatures of the CSs were computed using the Zanstra method (Zanstra 1931). The method, fully

developed by Harman & Seaton (1966) and extensively used in the literature (i.e., Kaler 1983), derives the total ionizing flux of the star by comparing the flux of a nebular recombination line of hydrogen or helium with the stellar continuum flux in the V band. The method assumes a particular choice of stellar spectral energy distribution, which from now on we consider to be a blackbody. The Zanstra method also assumes that all the photons above the Lyman limit of H or He^+ are absorbed within the nebula and that each recombination results in a Balmer series photon; therefore, when the He II 4686 Å line flux is available, the Zanstra method gives two values of the stellar temperature.

The data needed for the temperature calculation were taken from Paper II ($H\beta$ fluxes, nebular radii, and extinction constants) except for SMP 33, SMP 42, SMP 50, SMP 52, SMP 56, and SMP 63, for which the $H\beta$ fluxes were taken from Meatheringham, Dopita, & Morgan (1988b). The He II 4686 Å line fluxes were taken from Boroson, & Liebert (1989), Meatheringham & Dopita (1991b), Vassiliadis et al. (1992), Jacoby & Kaler (1993), and Monk, Barlow, & Clegg (1988). The line intensities given in some of these references were corrected for extinction, so we have uncorrected these fluxes by using the extinction constants given in the original references and the average Galactic reddening curve of Savage & Mathis (1979). To assure the best results we have been very conservative with the errors in the fluxes quoted by the references. We have supplemented the above with fluxes from our unpublished ground-based observations for SMP 33, SMP 56, SMP 100, SMP 102, SMP 34, and SMP 80 (R. A. Shaw et al. 2003, in preparation; S. Palen et al. 2003, in preparation). Table 2, column (4) we list the He II 4686 Å line intensity (and error) relative to $H\beta = 100$, not corrected for extinction; in column (5) we list the reference code for the He II fluxes.

4.1. Bolometric Corrections and LMC Distance Estimates

We computed bolometric luminosities for the CSs in our sample. The bolometric correction (BC) dependence with $T_{\rm eff}$ was taken from Vacca, Garmany, & Shull (1996), which was derived for Galactic O-type and early B-type stars. We use this relation since the dependence of the BC on $\log g$ was found to be extremely weak. Flower (1996) also found that each luminosity class appears to follow a unique BC-$T_{\rm eff}$ relation. The BCs have been computed by using the He II Zanstra temperature when available, otherwise the H I Zanstra $T_{\rm eff}$ was used. Temperatures from T_Z(He II) are the most reliable because of the likely optical thickness of most PNs to He II–ionizing photons. T_Z(H) can be reliable for PNs with sufficient optical depth; the problem is to determine which PNs are optically thick to hydrogen-ionizing radiation. The derived BCs agree with the empirical values given by Code et al. (1976).

To compute the CS luminosities we adopted a distance to the LMC of 50.6 kpc and an absolute bolometric magnitude for the Sun of $M_{\rm bol,\odot} = 4.75$ mag (Allen 1976). We estimated the error introduced in the derivation of the luminosity due to the distance variation caused by the depth of the LMC. The LMC can be considered a flattened disk with a tilt of the LMC plane to the plane of the sky of $34\overset{\circ}{.}7$ (van der Marel & Cioni 2001). Freeman, Illingworth, & Oemler (1983) derived a scale height of 500 pc for an old disk population. The scale height of young objects is between 100 to 300 pc (Feast 1989). From the three-dimensional structure

---

[5] The lower temperature limit is set to provide enough ionizing photons, and the upper limit is taken from the CS evolutionary tracks of Vassiliadis & Wood (1994).

TABLE 2
Magnitudes, Extinction, and He ii Fluxes

Name (1)	$V \pm \sigma$ (2)	$E(B-V)$ (3)	$I(\text{He \textsc{ii}}) \pm \sigma$ (4)	Reference (5)
J 41	19.88 ± 0.07	0.00	8 ± 4	1
SMP 4	21.19 ± 0.08	0.09	38.10 ± 3.81	2
SMP 9	$\geq 22.18, \geq 22.35^a$	0.16	39.5 ± 3.91	2
SMP 10	20.72 ± 0.07	0.11	5.0 ± 1	2
SMP 13	21.80 ± 0.19	0.06	42.17 ± 2.1	3
SMP 16	$\geq 22.15, \geq 21.74^a$	0.10	69.75 ± 3.5	3
SMP 18	18.97 ± 0.07	0.05	0.0	2
SMP 19	$22.25 \pm 0.43, \geq 20.38^a$	0.13	45.15 ± 2.3	3
SMP 25	$16.73^b \pm 0.09$	0.09	0.0	4
SMP 27	18.68 ± 0.06	0.04	0.0	5
SMP 28	...	0.23	...	...
SMP 30	$24.38 \pm 0.28, \geq 23.67^a$	0.08	...	...
SMP 31	17.04 ± 0.05	0.38	0.0	6
SMP 33	$\geq 20.08^a$	0.26	44.8 ± 4	5
SMP 34	17.93 ± 0.08	0.04	20.6 ± 4	7
SMP 42	$19.03^a \pm 0.02$	0.16	7.8 ± 0.8	3
SMP 46	$\geq 21.42, \geq 21.00^a$	0.13	31.5 ± 1.6	3
SMP 50	$18.89^a \pm 0.07$	0.13	19.0 ± 1	6
SMP 52	$19.84^a \pm 0.16$	0.20	25.0 ± 1.25	6
SMP 53	$\geq 18.42, \geq 18.01^a$	0.09	0.0	8
SMP 56	$17.79^a \pm 0.01$	0.08	0.4 ± 0.08	5
SMP 58	...	0.08	1.8 ± 0.18	6
SMP 59	20.10 ± 0.06	0.00	80.9 ± 8.09	5
SMP 63	$17.58^a \pm 0.04$	0.16	0.0	6
SMP 65	18.11 ± 0.05	0.16	0.0	6
SMP 71	≥ 18.67	0.17	39.9 ± 4	8
SMP 78	$\geq 17.34^b, \geq 17.54^a$	0.15	29.6 ± 1.5	3
SMP 79	≥ 17.23	0.13	...	...
SMP 80	18.24 ± 0.09	0.06	0.0	7
SMP 81	$16.38^b \pm 0.05$	0.17	0.0	8
SMP 93	≥ 25.55	0.00	52.4 ± 5.2	8
SMP 94^c	$15.22^b \pm 0.04$	0.74	54.7 ± 2.7	6
SMP 95	≥ 23.40	0.08	28.6 ± 4.3	2
SMP 100	21.84 ± 0.19	0.014	38.7 ± 3.9	5
SMP 102	22.15 ± 0.19	0.00	75.4 ± 7.5	5

Note.—The symbol $\geq$ refers to lower limit to the magnitude when the CS is not detected.
[a] WFPC2 data.
[b] CS saturated.
[c] Probably not a PN.
References.—(1) Boroson, & Liebert 1989; (2) Vassiliadis et al. 1992; (3) Meatheringham & Dopita 1991b; (4) Jacoby & Kaler 1993; (5) R. A. Shaw et al. 2003, in preparation; (6) Meatheringham & Dopita 1991a; (7) S. Palen et al. 2003, in preparation; (8) Monk et al. 1988.

of the galaxy, we have a spread in the distance modulus of 0.03, which we propagate into the error of the absolute magnitudes and luminosities. We have not taken into account the errors in the distance to the LMC, since it will affect all the objects in the same way.

We give our resulting temperatures and luminosities in Table 3. In column (1) we give the PN name; in columns (2) and (3) we give the effective temperatures (in units of 10^3 K) derived from the Zanstra method for the He ii and the hydrogen recombination lines, respectively. The two luminosity determinations given by the Zanstra method are given in columns (4) and (5), respectively. If the CS was not detected we give the upper limit of the luminosity. The visual absolute magnitude and the stellar luminosity (derived from the BC) are listed in columns (6) and (7), respectively. The BCs and their errors, computed by propagating the

errors in the determination of $T_{\rm eff}$, are given in column (8). All the values are listed with their respective errors.

5. RESULTS

In the following discussion we use the morphological classification of the nebulae provided in Paper II. PNs are classified as round, elliptical, bipolar, bipolar core, and point-symmetric according to their morphology in the [O iii] 5007 Å line. In those cases for which we have two measurements of the magnitude, we have selected one of them according to the following criteria: for SMP 9, SMP 16, SMP 46, and SMP 53 we have used the STIS lower limits on magnitudes since they are deeper observations, for SMP 19 and SMP 30 we used the STIS data because the CSs are detected with this instrument, and in the case of SMP 78 we

TABLE 3

CS PARAMETERS

Name (1)	$T_{\rm eff}({\rm He\,II}) \pm \sigma$ $(10^3\,{\rm K})$ (2)	$T_{\rm eff}({\rm H}) \pm \sigma$ $(10^3\,{\rm K})$ (3)	$(\log L_Z/L_\odot) \pm \sigma$ He II (4)	$(\log L_Z/L_\odot) \pm \sigma$ H (5)	$M_V \pm \sigma$ (6)	$(\log L_Z/L_\odot) \pm \sigma$ (7)	$BC \pm \sigma$ (8)
J 41	60.1 ± 3.5	30.4 ± 1.8	3.24 ± 0.07	2.47 ± 0.06	1.36 ± 0.07	3.37 ± 0.07	−5.03 ± 0.17
SMP 4	89.9 ± 7.2	48.1 ± 7.4	3.31 ± 0.09	2.56 ± 0.17	2.67 ± 0.08	3.32 ± 0.10	−6.23 ± 0.24
SMP 9	114.0 ± 10.2	77.6 ± 13.7	≤3.29	≤2.89	≥3.66	≤3.25	−6.93 ± 0.27
SMP 10	74.6 ± 4.3	57.1 ± 7.9	3.31 ± 0.07	2.98 ± 0.15	2.20 ± 0.07	3.29 ± 0.07	−5.67 ± 0.17
SMP 13	129.1 ± 11.9	99.1 ± 18.2	3.49 ± 0.11	3.16 ± 0.20	3.28 ± 0.19	3.51 ± 0.13	−7.30 ± 0.27
SMP 16	141.9 ± 17.3	97.5 ± 21.8	≤3.45	≤3.07	≥3.62	≤3.54	−7.58 ± 0.36
SMP 18	...	30.9 ± 2.8	...	2.91 ± 0.09	0.45 ± 0.07	2.94 ± 0.11	−3.05 ± 0.27
SMP 19	143.5 ± 17.5	119.1 ± 27.9	3.52 ± 0.12	3.29 ± 0.21	3.73 ± 0.43	3.45 ± 0.23	−7.61 ± 0.36
SMP 25[a]	...	33.7 ± 2.6	...	3.95 ± 0.08	−1.79 ± 0.09	3.94 ± 0.10	−3.31 ± 0.23
SMP 27	...	28.3 ± 2.9	...	2.92 ± 0.10	0.16 ± 0.06	2.95 ± 0.13	−2.79 ± 0.31
SMP 28[b]	...	17.1 ± 1.1	...	4.14 ± 0.05	...	...	...
SMP 30	...	149.3 ± 37.8	...	2.66 ± 0.27	5.86 ± 0.28	2.65 ± 0.32	−7.73 ± 0.75
SMP 31	...	28.6 ± 2.4	...	4.01 ± 0.08	−1.48 ± 0.05	3.62 ± 0.10	−2.82 ± 0.25
SMP 33	110.9 ± 11.2	69.7 ± 13.8	≤4.16	≤3.64	≥1.55	≤4.06	−6.85 ± 0.30
SMP 34	67.8 ± 3.6	32.0 ± 2.9	4.22 ± 0.06	3.35 ± 0.10	−0.59 ± 0.08	4.29 ± 0.07	−5.38 ± 0.16
SMP 42	66.4 ± 0.8	37.7 0.3	3.89 ± 0.02	3.23 ± 0.01	0.51 ± 0.02	3.82 ± 0.02	−5.32 ± 0.03
SMP 46	119.4 ± 35.4	93.8 ± 55.4	≤3.20	≤2.84	≥2.90	≤3.65	−7.07 ± 0.88
SMP 50	80.4 ± 0.9	46.0 ± 0.8	4.15 ± 0.02	3.49 ± 0.01	0.37 ± 0.07	4.11 ± 0.03	−5.89 ± 0.03
SMP 52	100.9 ± 2.6	69.8 ± 3.5	4.13 ± 0.04	3.68 ± 0.01	1.32 ± 0.16	4.00 ± 0.07	−6.57 ± 0.08
SMP 53	...	43.2 ± 4.1	...	≤0.60	≥−0.1	≤3.63	−4.04 ± 0.28
SMP 56	45.9 ± 2.0	29.0 ± 3.1	3.85 ± 0.05	3.35 ± 0.10	−0.74 ± 0.02	3.89 ± 0.05	−4.23 ± 0.13
SMP 58[b]	71.4 ± 2.8	71.4 ± 8.4	3.49 ± 0.05	3.49 ± 0.13	...	...	...
SMP 59	98.2 ± 6.8	46.2 ± 5.6	3.75 ± 0.08	2.85 ± 0.13	1.58 ± 0.06	3.86 ± 0.09	−6.49 ± 0.21
SMP 63	...	38.8 ± 0.4	...	3.85 ± 0.01	−0.94 ± 0.04	3.77 ± 0.02	−3.73 ± 0.03
SMP 65	...	27.0 ± 2.2	...	3.25 ± 0.08	−0.41 ± 0.06	3.12 ± 0.10	−2.65 ± 0.24
SMP 71	83.4 ± 5.2	40.8 ± 4.8	≤4.34	≤3.53	≥0.15	≤4.27	−6.00 ± 0.18
SMP 78	75.7 ± 3.1	36.4 ± 2.8	≤4.67	≤3.82	≥−0.99	≤4.61	−5.71 ± 0.12
SMP 79	...	33.5 ± 2.6	...	≤3.80	≥−1.30	≤3.79	−3.29 ± 0.23
SMP 80	...	30.7 ± 2.8	...	3.21 ± 0.09	−0.28 ± 0.10	3.22 ± 0.12	−3.03 ± 0.27
SMP 81[a]	...	28.1 ± 1.7	...	3.99 ± 0.07	−2.14 ± 0.06	3.86 ± 0.08	−2.77 ± 0.18
SMP 93	372.4 ± 97.6	526.0 ± 158.5	≤3.25	≤3.73	≥7.03	≤3.04 ± 0.39	−10.45 ± 0.78
SMP 94[a]	59.3 ± 2.6	21.1 ± 1.4	6.00 ± 0.05	4.88 ± 0.06	−3.30 ± 0.05	5.21 ± 0.06	−4.99 ± 0.13
SMP 95	146.2 ± 28.6	152.4 ± 57.1	≤2.81	≤2.93	≥4.88	≤3.08	−7.67 ± 0.58
SMP 100	127.1 ± 11.7	99.5 ± 18.3	3.39 ± 0.11	3.09 ± 0.20	3.31 ± 0.19	3.47 ± 0.13	−7.25 ± 0.27
SMP 102	131.8 ± 12.4	82.4 ± 14.2	3.30 ± 0.11	2.72 ± 0.18	3.63 ± 0.19	3.39 ± 0.14	−7.36 ± 0.28

Note.—The symbol ≥ refers to lower limit to the magnitude when the CS is not detected. Luminosities for those cases are therefore upper limits and are preceded by ≤.

[a] The photometry was performed on saturated data.

[b] Temperature and luminosity for this nebula were derived from crossover analysis. The temperatures should be considered upper limits.

used the WFPC2 data because the STIS data are saturated. All saturated and unresolved objects have been excluded from the following analysis.

5.1. *Effective Temperatures*

In Figure 1 we plot the Zanstra ratio $T_Z({\rm He\,II})/T_Z({\rm H})$ versus $T_Z({\rm He\,II})$, but only for those objects for which the CS was clearly detected (i.e., no limiting values were used) and for which $T_Z({\rm He\,II})$ and $T_Z({\rm H})$ are the Zanstra temperatures derived from the He II 4686 Å and the Hβ recombination lines, respectively. The difference between the two temperature determinations is a well-known effect: the " Zanstra discrepancy " (Kaler 1983; Kaler & Jacoby 1989; Gathier & Pottasch 1988). The Zanstra discrepancy has been studied by several authors; the optical thickness in the nebula to the H- and He⁺-ionizing radiation is the principal reason cited for $T_Z({\rm He\,II})$ often exceeding $T_Z({\rm H})$ (Kaler & Jacoby 1989; Stasinska & Tylenda 1986; Schönberner & Tylenda 1990; Gruenwald & Viegas 2000). We find that the Zanstra ratio

approaches unity for higher effective temperatures, in agreement with the previous results cited above. SMP 10 and SMP 56 (the only filled circle and the only open circle, respectively) are the only objects that have both a small Zanstra ratio and a low effective temperature. Both objects have a small He II flux, which can indicate either that the nebula is optically thick to both hydrogen and helium radiation or that the He II Zanstra calculation is rather uncertain. SMP 10 is also the only point-symmetric object in this sample, and SMP 56 the only round PN in the plot. It might be significant that both fall off the trend. Although the number of objects is too small to be conclusive, we do not find any morphological segregation of the Zanstra discrepancy in Figure 1, with the exceptions of SMP 10 and SMP 56.

Villaver, Manchado, & García-Segura (2002b) found that the transition from an optically thick to an optically thin nebula depends on the initial mass of the star: the higher the initial mass, the higher the effective temperature at which the nebula becomes optically thin. If the Zanstra discrepancy is due only to the optical thickness in the H-ionizing
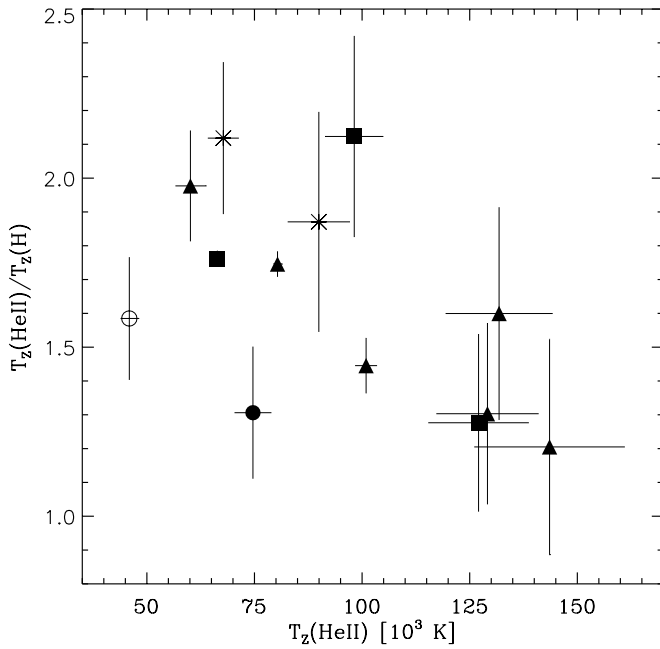
FIG. 1.—Ratio of Zanstra temperatures vs. the He II Zanstra temperature. The symbols represent the morphological types of the hosting nebulae: round (*open circle*), elliptical (*asterisks*), bipolar and quadrupolar (*squares*), bipolar core (*triangles*), and point-symmetric (*filled circle*).

radiation and since the Zanstra ratio approaches unity for higher effective temperatures, then, according to the results of Villaver et al. (2002b), it is very likely that the objects with the higher Zanstra discrepancy have low-mass progenitors. We return to this point in § 6.

5.2. *Luminosities*

In the adopted Zanstra method, the stellar temperature is computed by determining the point where a parameterization of the stellar luminosity with temperature (based on a blackbody assumption and on the measured visual magnitude and extinction) equals the parameterization for the luminosity of the nebula in two different recombination lines; thus, the Zanstra method gives as a by-product two determinations of the stellar luminosity: from the hydrogen and the He II temperatures. The Zanstra method does not use any empirical bolometric correction to convert the magnitude in the visual band to the bolometric magnitude, but it is instead a function of the stellar temperature, which itself is based on a blackbody assumption.

The CSPNs in the LMC are free of the distance uncertainty that dominates the determination of CSs luminosities for Galactic PNs. However, another problem remains: the measurement of the T_{eff} that influences the luminosity determination through the BC. We have the stellar luminosities derived from the Zanstra method (L_Z) and those derived from the observed magnitudes by using the BCs (L_*). Although the T_{eff} plays a role in both determinations, they are not completely independent, and we can compare them to check the consistency of luminosity determinations based on these two approaches.

In Figure 2 we show the $\log L_*/L_\odot$ versus the $\log L_Z/L_\odot$ derived from He II (*left*) and H I (*right*) Zanstra analysis. We are comparing the two luminosity determinations in a self-consistent way, and the luminosities derived by using the He II Zanstra temperature to determine the BC are compared with those luminosities derived from the He II Zanstra analysis (*left*). The same comparison is valid for the luminosities derived from hydrogen Zanstra temperatures. These are plotted in Figure 2 (*left*), but only for those CSs for which the
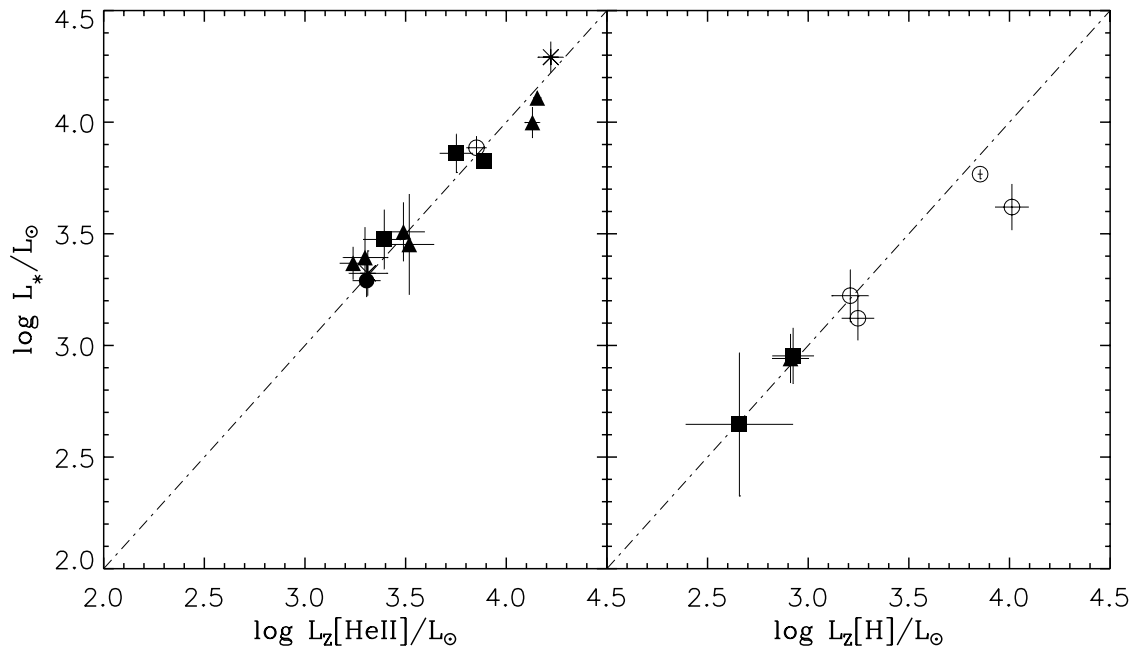

FIG. 2.—*Left*, Stellar luminosity derived from the observed magnitude (in solar units logarithm scale) against Zanstra luminosity from He II temperature (T_Z[He II]); *right*, same but against the Zanstra luminosity derived from hydrogen temperature (T_Z[H]). The symbols represent the morphology of the hosting nebulae and are as in Fig. 1. The dotted lines represents the 1 : 1 relation.

He II Zanstra temperature was not available. Figure 2 shows that the points lie very close to the 1 : 1 relation.

The two samples of CSs displayed in the left and right panels of Figure 2 show a quite different luminosity range. The CSs displayed in Figure 2 (left), those for which we have a He II Zanstra temperature, appear to be more luminous than the CSPNs with hydrogen Zanstra temperatures (Fig. 2, right). Here T_Z(He II) is thought to represent more closely the effective temperature of the star, and it is rather well established that T_Z(H) is probably underestimating the CS temperature for optically thin objects. CSs with higher effective temperature will have bigger BCs and therefore more likely higher luminosities, and thus if the T_Z(H) is underestimated is likely that the CS luminosities will be underestimated too. However, we do not think that the lower luminosity range of the CSs in Figure 2 (left) is due to this effect. The absence of 4686 He II line emission in these nebulae suggests that the CSs have a low temperature, which is indeed the case (i.e., the CSs are not hot enough to

ionize He II); therefore, we are more inclined to think that most of the CSs plotted in Figure 2 (right) are intrinsically low-luminosity stars. It should be mentioned that He II 4686 fluxes of only 0.005 of Hβ can yield significantly higher T_Z(He II) than T_Z(H) Zanstra effective temperatures. He II 4686 line fluxes are rarely available at this accuracy; thus, the distribution in the $\log L$–$\log T$ plane could change significantly with higher quality spectra.

Figure 3 shows L_*, T_Z, and the nebular radius plotted (top to bottom) versus the relative difference between L_* and L_Z on a linear scale. The left and right panels of Figure 3 represent the relative differences in the luminosity when derived from the He II and H I Zanstra analysis, respectively. In the left panel of Figure 3 we plot only those objects for which an He II Zanstra temperature is available. In the right panel of Figure 3 we plot the CSs with only hydrogen Zanstra temperatures, i.e., only the CSs for which the He II λ4686 flux relative to Hβ is zero or not available. We find that all the L_Z(He II) are within $\sim$30% of the L_*. We do not
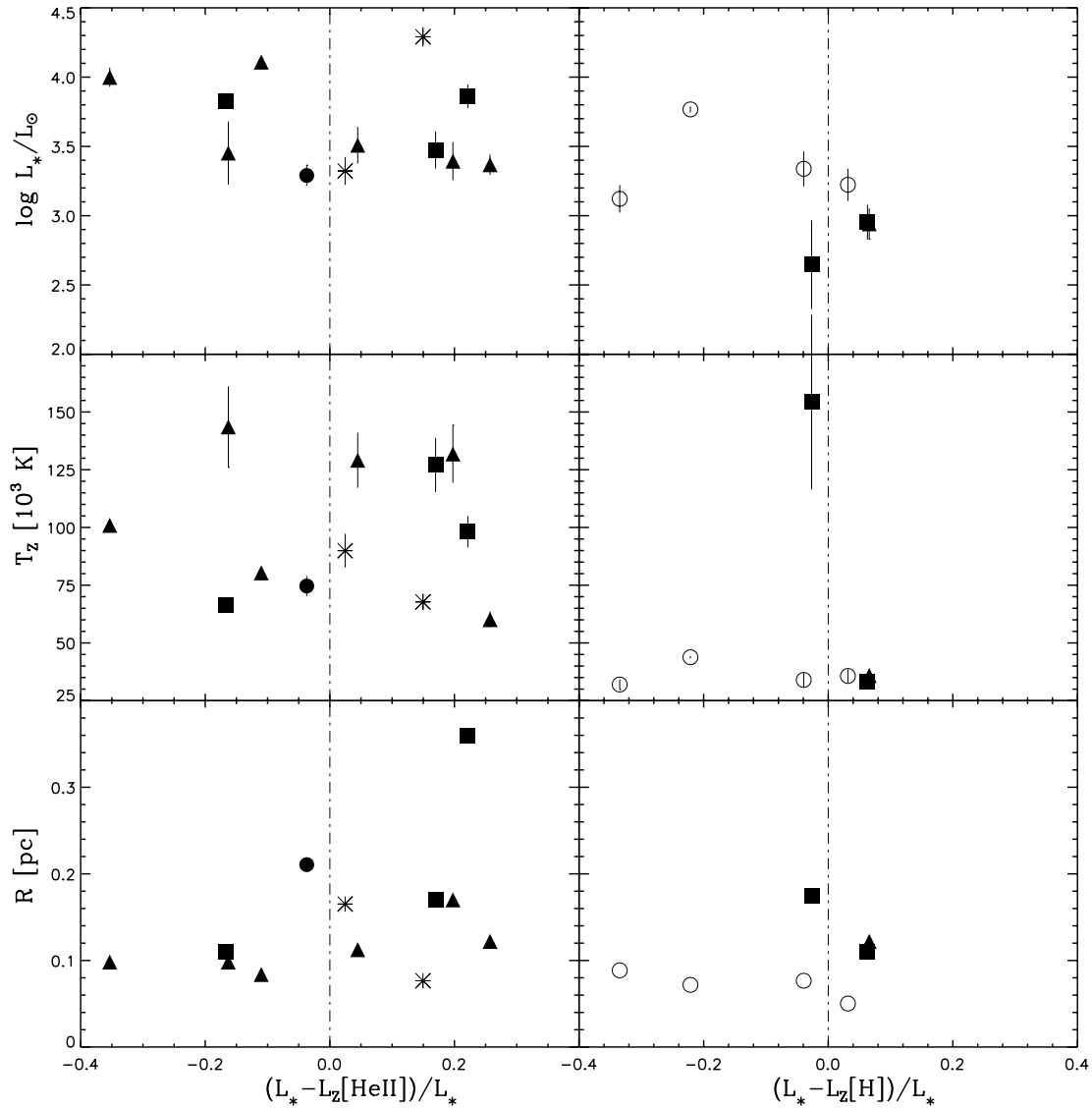

Fig. 3.—Relative differences between the observed, L_*, and derived Zanstra luminosities vs. $\log L_*/L_\odot$, Zanstra temperature, and nebular photometric radius, showing luminosities derived from the He II (left) and H I (right) Zanstra temperatures. The symbols are as in Fig. 1, and the dotted lines represent equal luminosity.

find any systematic differences with L_*, with T_Z(He II), nor with the nebular radius or morphology. The L_Z(H) and L_* agree to within 20%, with the exception of two objects (SMP 63 and SMP 65), which are within 40%. SMP 31 is not shown in the plots because of the high $(L_*-L_Z[H])/L_* \sim 150\%$. It could be that there are systematic errors in the $(L_*-L_Z[H])/L_*$ difference, but this is not conclusive because of the small number of data points. As mentioned before, the dependency of the BC with T_{eff} is based on an empirical approach, while in the Zanstra analysis the relation between the luminosity and T_{eff} is based on a blackbody assumption. We find that both determinations provide similar values (within ~30%) of the CS luminosity.

5.2.1. *Luminosity–Nebular Radius and Surface Brightness Relations*

The relation between CSs and the nebulae is explored in Figure 4, where we show the $\log L_*/L_\odot$ versus the nebular photometric radius (taken from Paper II). The photometric radius and the CS luminosity should be good indicators of the evolutionary status of the nebula and the CS, respectively. On one hand, the evolution of the nebular radius is a gasdynamic problem that depends, among other things, on the energy that the stellar wind is injecting into the gas, which is a function of the evolution of the stellar luminosity and the core mass. On the other hand, the stellar luminosity, after a constant phase for hydrogen burners, decreases during the evolution at a rate that depends mainly on the core mass; thus, it is expected that both quantities decrease with time and that they do not evolve independently; the evolution of the radius must be related to that of the luminosity of the CS.

We find in Figure 4 a tendency of higher radii for lower stellar luminosities. There is an apparent segregation in

Figure 4 of smaller nebular radii for symmetric PNs for which a selection effect toward the detection of younger symmetric PNs cannot be ruled out. Villaver et al. (2002b) studied the PN formation for a range of progenitor masses and followed the gas structure that resulted from the AGB evolution (Villaver, García-Segura, & Manchado 2002a). To have an indication of how the nebular evolution relates to the evolution of the CS we have superposed on Figure 4 an interpolation of the nebular radius evolution with the CS luminosity for different progenitors from the numerical simulations of Villaver et al. (2002b).

A qualitative comparison with the models shows that high-luminosity objects with large radius may have a low-mass progenitor star because of the fast evolution of the CS luminosity for high-mass progenitors. The nebular radius does not evolve as fast as the luminosity, although the amount of energy injected by the wind is higher.

A quantitative comparison with the models shown is not possible, since the core mass, stellar luminosity, stellar wind history, and gasdynamical evolution are dependent on the metal content of the gas and star. A different metallicity will change the efficiency of the wind-driven mechanism and the cooling of the gas. Work is in progress on numerical simulations of PN formation that reflect the metallicity of the clouds. We would like to point out here that, once the models are performed for the LMC metallicity, a plot such as the one shown in Figure 4 will be very useful to constrain the wind energy injected during the post-AGB phase by the star.

Figure 5 shows two direct observational quantities in the LMC: the absolute visual magnitude and the nebular radius (in logarithmic scale). There is a strong correlation between the absolute visual magnitude and the nebular radius. An evolutionary effect is a very likely explanation for this correlation since as the CS fades, the radius becomes bigger. There is also a strong correlation with nebular morphology, at least for symmetric versus asymmetric types. In Paper I,
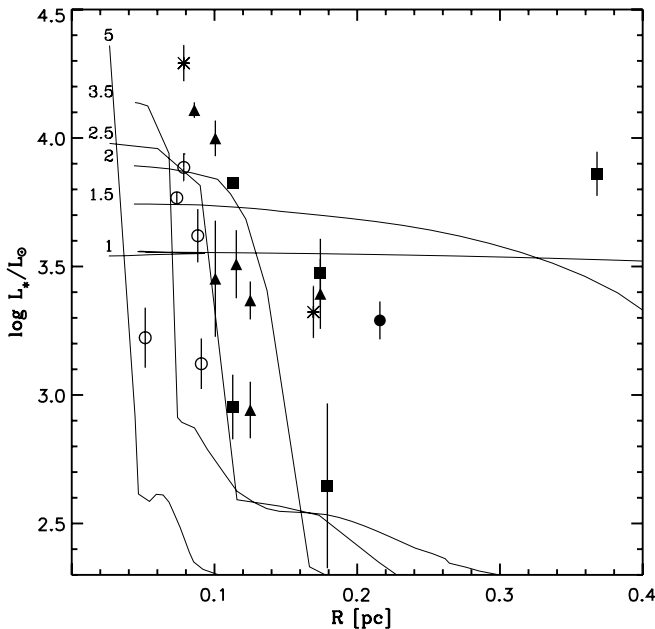

FIG. 4.—Logarithm of the observed luminosity vs. the physical radius of the nebulae. The symbols are as in Fig. 1. The solid lines represent the evolution of the nebular radius vs. the stellar luminosity taken from the numerical simulations of Villaver, Manchado, & García-Segura (2002b) for Galactic PNs. Each line has been marked with the initial mass of the progenitor used in the hydrodynamical simulations.
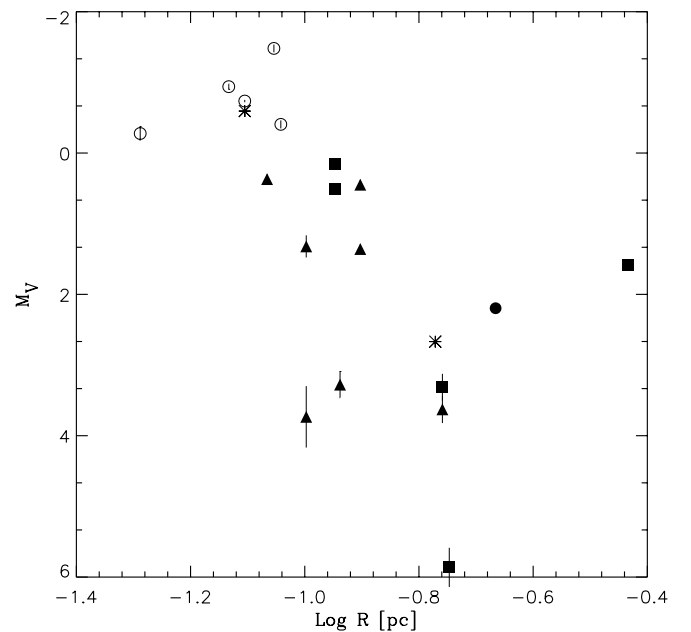

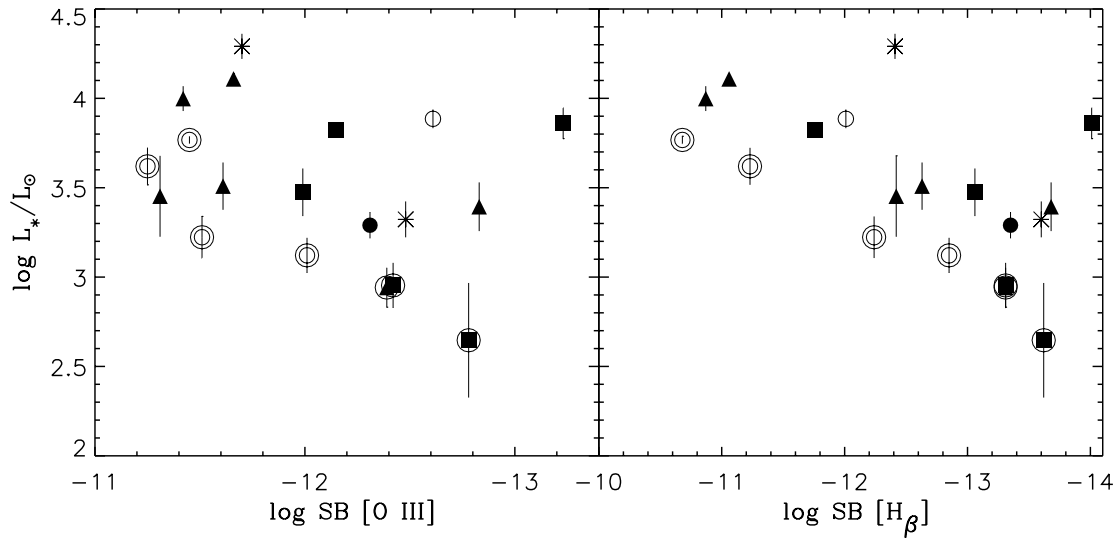FIG. 5.—Absolute visual magnitude vs. the physical radius of the nebulae. The symbols are as in Fig. 1.

FIG. 6.—Logarithm of the observed luminosity vs. the surface brightness of the nebula in the [O III] and Hβ lines. The symbols are as in Fig. 1. The objects with hydrogen Zanstra temperatures have been surrounded with a circle.

Shaw et al. noted the tendency of round nebulae to have systematically lower expansion velocities, and they may therefore be older than their relative sizes would suggest. However, their small size and visually bright CSs might imply that they are young; thus, using the nebular radius and visual magnitude as the sole indicators of their evolutionary state may be too simplistic. We shall address the complicated interpretation of nebular kinematics in this context in a future paper.

In Figure 6 we plot the CS luminosity versus the nebular surface brightness in the Hβ emission line ($SB_{H\beta}$, defined as the integrated line flux divided by the nebular area πR^2_{phot}). The luminosity gradient steepens as $SB_{H\beta}$ declines, as expected by the common evolution of nebulae and stars. We do not find any low-SB object with high luminosity, nor any object with low CS luminosity and high SB, with the exception of SMP 59 (the square point in the right upper corner of the plots). The relation is shown in Figure 6 (left) for the [O III] line (the [O III] SB has been taken from Paper II). The fact that the relation is the same, although with higher dispersion (which might be due to variations in oxygen abundance), for a collisionally excited (rather than recombination) emission line strengthens the point that a fundamental physical process, related to nebular evolution, must underlie the cause.

In Figure 7 we have added to the luminosity versus $SB_{H\beta}$ plot those points for which we have only a lower limit to the magnitudes (arrow), and we have surrounded each point with a circle of size proportional to the nebular radius. Low-SB objects are always located toward the position of low-luminosity CSs and have a larger radius. The potential use of this kind of plot as an indicator of the nebular age is very clear. We find that it offers a better diagnostic than the H-R diagram for showing the evolutionary status of the nebula, confirming that an evolutionary effect must underlie the SB–nebular radius relations found in Papers I and II.

5.3. Stellar Distribution on the log L–log T Plane

Figure 8 shows the distribution on the log L–log T plane of the CSs of those PNs in our sample for which the CS was

detected. The evolutionary tracks have been taken from Vassiliadis & Wood (1994) for stars with LMC metallicity. The post-AGB evolution of a CSPN depends on its previous AGB evolution and on the phase of the thermal pulse cycle on which the star leaves the AGB (Schönberner 1983; Vassiliadis & Wood 1994; Blöcker 1995). Whether the star leaves the AGB when helium shell– or hydrogen shell–burning is dominant determines the He- or H-burning nature of the subsequent post-AGB track. The lower mass models presented by Vassiliadis & Wood (1994) are more efficient at producing He-burning post-AGB tracks, which they
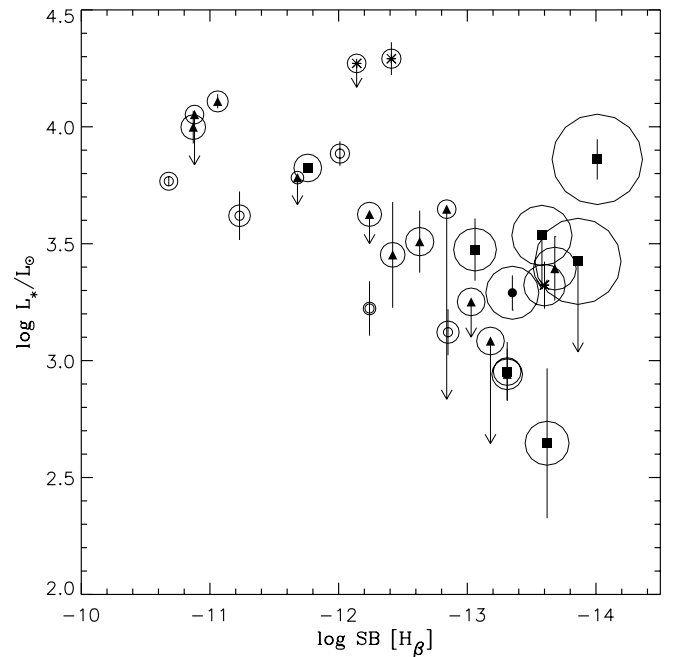

FIG. 7.—Same as Fig. 6 but only for the Hβ line. We have also plotted the upper limits of the luminosity for those objects for which the CS was not detected. The arrows mean that the magnitude was a lower limit, and so the luminosity is an upper limit. Each data point is surrounded by a circle proportional to the radius of the hosting nebula.
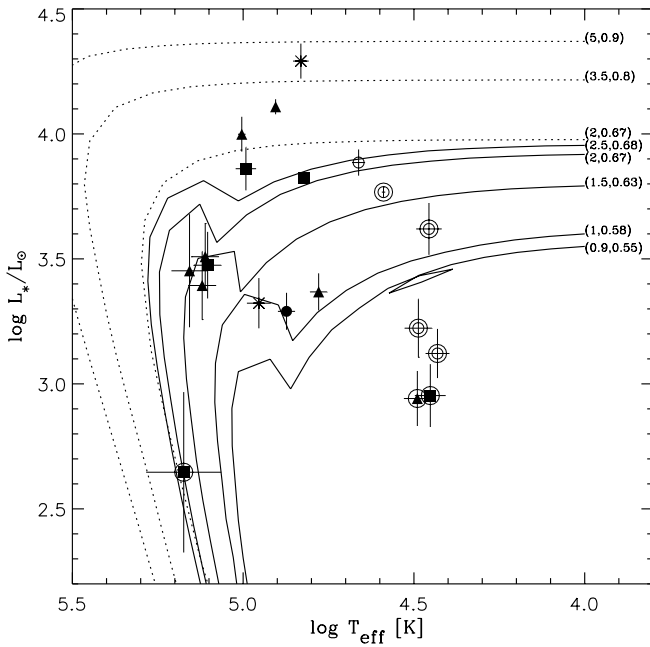
Fig. 8.—H-R diagram for the CSPNs. Symbols are as in Fig. 1. We have surrounded by a circle those points for which the H I Zanstra temperatures have been used. Evolutionary tracks are for LMC metallicities from Vassiliadis & Wood (1994). The initial and core masses are marked on each track. The solid lines are for He burners, and the dotted lines for hydrogen burners.

TABLE 4
STELLAR MASSES

Name	Morphology	M ($M_\odot$)	Comments
J 41	E(bc)	0.59	Interpolation of He-burning tracks
SMP 4	E	0.58	He-burning track
SMP 10	P	0.58	He-burning track
SMP 13	R(bc)	0.63	He-burning track
SMP 19	E(bc)	0.63	He-burning track
SMP 30	B	0.67[a]	He-burning track
		0.67[a]	H-burning track
SMP 31	R	0.59[a]	Interpolation of He-burning track
SMP 34	E	0.84	L-core mass relation H-burning tracks
SMP 42	Q	0.67	Interpolation of He-burning tracks
SMP 50	E(bc)	0.75	Interpolation of H-burning tracks
SMP 52	R(bc)	0.70	Interpolation of H-burning tracks
SMP 56	R	0.68	He-burning track
SMP 59	Q	0.65	Extrapolation of H-burning tracks
		0.69	Extrapolation of He-burning tracks
SMP 63	R	0.64[a]	Interpolation of He-burning tracks
SMP 100	Q	0.63	He-burning track
SMP 102	E(Bc)	0.60	Extrapolation of He-burning tracks

[a] Derived from hydrogen Zanstra analysis and therefore rather uncertain (see text). Note that the masses derived from He-burning tracks might be slightly smaller if they were derived from H-burning tracks.

argue is a natural consequence of the mass-loss behavior during the AGB phase. The mass-loss rates on the AGB were artificially enhanced or diminished to control the point of departure from the AGB in the He-burning track models for initial masses 1.5 and 2 $M_\odot$. It is important to note that the mechanism that controls the departure of the star from the AGB is unknown and therefore artificially defined in the stellar evolutionary models.

We do not find the tendency reported by Dopita et al. (1996) of size evolution along the evolutionary tracks on the H-R diagram. We do find that the luminosity versus SB diagram is a better diagnostic of the evolutionary status of the nebula. It is important to note that the masses derived by Dopita et al. (1996) and Vassiliadis et al. (1998) are based on photoionization modeling of the optical spectrophotometry of individual nebulae. The conclusions about the helium- and hydrogen-burning nature of the progenitors are based on a comparison between the dynamical ages derived from observations of the nebula and a determination of the theoretical timescale. The theoretical timescale was obtained through an empirical fit to the expansion velocity as a function of the position on the H-R diagram and theoretical evolutionary tracks of the CS. The physical relationship between the expansion velocity of the nebula and the CS luminosity is a problem that requires numerical simulations to be solved.

The same kind of distribution on the H-R diagram that Shaw & Kaler (1989) called "Zanstra's wall," that is, the apparently high number of CSs with $4.9 \leq \log T_{\rm eff} \leq 5.1$, can be seen in Figure 8, although the number of objects is very small. As pointed out by Shaw & Kaler (1989), it is very possible that the nebula becomes optically thin to He II radiation above a certain stellar temperature, in which case the

Zanstra method provides only lower limits of the temperature for the hottest CSs.

We have derived the core masses based on the locations of the post-AGB tracks at hand and the interpolations between them. We have not derived core masses for the four points that lie below the tracks. Only hydrogen Zanstra temperatures could be computed for those objects, and therefore their temperatures are very likely to be underestimated. If their temperatures were higher, those points would move toward the upper left of the H-R diagram (the BC will increase and therefore so will the derived luminosity), where the theoretical stellar evolutionary tracks predict the evolution of most CSPNs. Another, albeit very unlikely possibility, is that those objects are the result of the evolution of a progenitor less massive than the lower mass progenitor available in the models of Vassiliadis & Wood (1994), e.g., 0.9 $M_\odot$.

The core masses and the morphological classification of the nebulae are summarized in Table 4. We do not find any correlation between the mass of the CS and the morphology of the nebula. The mean and the median of the mass distribution are 0.65 and 0.64 $M_\odot$, respectively. The number of objects is small, and therefore the distribution of the objects in the H-R diagram has limited statistical value. However, this is the first time ever that CSPN masses have been derived without the distance bias affecting the Galactic PNs, so these averages are extremely valuable.

6. SUMMARY AND DISCUSSION

The distribution of CSPNs in the H-R diagram is rather uncertain for Galactic PNs, mainly for the lack of reliable distances. Because LMC PNs are seldom resolved from the ground, most of the previous determinations of CSPN masses are highly model-dependent; i.e., they are based on CS luminosities derived solely from nebular fluxes (Henry,

Liebert, & Boroson 1989; Monk et al. 1988; Kaler & Jacoby 1990, 1991; Dopita et al. 1996; 1997; Vassiliadis et al. 1998). Although *International Ultraviolet Explorer* spectra were employed in the work by Aller et al. (1987), the CSs were not detected, and therefore photoionization modeling was used to determine the CS parameters. In all, only four CS masses were previously determined from direct measurement of the stellar flux, and then only from the UV spectrum of the CS (Dopita et al. 1993; Bianchi et al. 1997). Dopita et al. (1993) estimated the mass of the CS of SMP 83 to be ∼1 $M_\odot$, an extremely massive object, which has been classified as a Wolf-Rayet nucleus by Peña et al. (1995). The CS masses determined by Bianchi et al. (1997) are in the range 0.62–0.68 $M_\odot$.

We have performed photometry and derived luminosities for a sample of CSs in the LMC. By observing LMC objects for which the distance is well known, we greatly reduce the uncertainty in the vertical axis of the H-R diagram; by directly measuring the CS continua with *HST*, we eliminate the dependency on photoionization models in the determination of the stellar flux. Although significant uncertainty remains in the determination of effective temperatures, we have adopted a very conservative approach by using for most cases only effective temperatures derived from the He II Zanstra analysis, which are considered more reliable.

The Zanstra discrepancy has been successfully explained on the basis of an optical depth effect (Kaler & Jacoby 1989; Gruenwald & Viegas 2000). Villaver et al. (2002b) showed an increased likelihood that PNs become optically thin at a lower effective temperature for lower mass progenitors. We find that most of the objects with high Zanstra discrepancy indeed have lower progenitor masses, confirming the optical depth effect as the main reason for the Zanstra discrepancy. However, two of our targets with high Zanstra discrepancies (SMP 34 and SMP 50) are among the most massive and youngest of the sample. It is very unlikely that these two nebulae are optically thin to hydrogen radiation, so some other effect, e.g., an excess of photons above the He II ionization threshold if the stars had pure H stellar atmospheres, must be invoked to explain the Zanstra discrepancy in these two objects.

We find an average mass for our sample of 0.65 $M_\odot$, which is close to (although slightly higher than) the average mass of white dwarfs in the Galaxy (Finley et al. 1997; Bergeron et al. 1992). Finley et al. (1997) pointed out that the average mass of white dwarfs should be used with caution as it depends on the underlying distribution of masses, which is a function of the temperature range covered by the sample. The total number of objects in our sample is very small so it would be premature to plot histograms of our distribution and assign great significance to the peak values of the sample. Work on the data of the *HST* SNAP program 9077 (in which ∼60 LMC objects were observed) is in progress and will help us to address this issue.

The mass loss during the AGB phase is expected to be affected by the metallicity, and the relation between the mass of a white dwarf and that of its progenitor on the main sequence tells us the complete integrated mass loss through the evolution. If mass loss is reduced in the LMC with respect to the Galaxy because of the lower metallicity, assuming that other selection effects are not operating, one might expect a change in the mass distribution of white dwarfs in the LMC compared with other metallicity environments. The mass distribution of the CSPNs should show the same effect. The star formation history of the LMC should also be reflected in the average mass of CSPNs. We plan to compare the mass distribution of the CSPNs in two different metallicity environments: the LMC and the Small Magellanic Cloud, which are free of the biases that make the comparison with the Galactic CSs very difficult.

We would like also to propose the LMC PNs as excellent tests probes to study the gasdynamic processes and wind injection rates. By comparing the correlations between the nebular radius and the stellar luminosity with numerical models pursued for LMC metallicities, we will be able to constrain the efficiency of the wind-driven mechanisms during the post-AGB phase. Finally we do not find any strong evidence of morphological segregation as a function of the progenitor mass, although this point will be explored further once we analyze a larger sample of objects already observed with the *HST*.

REFERENCES

Allen, C. W. 1976, Astrophysical Quantities (London: Athlone)
Aller, L. H., Keyes, C. D., Maran, S. P., Gull, T. R., Michalitsianos, A. G., & Stecher, T. P. 1987, ApJ, 320, 159
Amnuel, P. 1995, Ap&SS, 225, 275
Baggett, S., et al. 2002, in *HST* WFPC2 Data Handbook, Version 4.0, ed. B. Mobasher (Baltimore: STScI)
Bergeron, P., Saffer, R. A., & Liebert, J. 1992, ApJ, 394, 228
Bianchi, L., Vassiliadis, E., & Dopita, M. 1997, ApJ, 480, 290
Biretta, J. A., et al. 2002, WFPC2 Instrument Handbook, Version 7.0 (Baltimore: STScI)
Blöcker, T. 1995, A&A, 299, 755
Boroson, T. A., & Liebert, J. 1989, ApJ, 339, 844
Brown, T., et al. 2002, *HST* STIS Data Handbook, Version 4.0, ed. B. Mobasher (Baltimore: STScI)
Calvet, N., & Peimbert, M. 1983, Rev. Mexicana Astron. Astrofis., 5, 319
Code, A. D., Bless, R. C., Davis, J., & Brown, R. H. 1976, ApJ, 203, 417
Corradi, R. L. M., & Schwarz, H. E. 1995, A&A, 293, 871
Dolphin, A. E. 2000a, PASP, 112, 1397
———. 2000b, PASP, 112, 1383
Dominguez, I., Chieffi, A., Limongi, M., & Straniero, O. 1999, ApJ, 524, 226
Dopita, M. A., Ford, H. C., Bohlin, R., Evans, I. N., & Meatheringham, S. J. 1993, ApJ, 418, 804

Dopita, M. A., Ford, H. C., Bohlin, R., Evans, I. N., & Meatheringham, 1996, ApJ, 460, 320
———. 1997, ApJ, 474, 188
Feast, M. W. 1989, Recent Developments of Magellanic Cloud Research, ed. K. S. de Boer, F. Spite, & G. Stasinska (Paris: Observatoire de Paris), 75
Finley, D. S., Koester, D., & Basri, G. 1997, ApJ, 488, 375
Flower, P. J. 1996, ApJ, 469, 355
Freeman, K. C., Illingworth, G., & Oemler, A. 1983, ApJ, 272, 488
Gabler, R., Kudritzki, R. P., & Mendez, R. H. 1991, A&A, 245, 587
García-Segura, G., Langer, N., Różyczka, M., & Franco, J. 1999, ApJ, 517, 767
Gathier, R., & Pottasch, S. R. 1988, A&A, 197, 266
Gilliland, R. L., Goudfrooij, P., & Kimble, R. A. 1999, PASP, 111, 1009
Girardi, L., Bressan, A., Bertelli, G., & Chiosi, C. 2000, A&AS, 141, 371
Gorny, S. K., Stasinska, G., & Tylenda, R. 1997, A&A, 318, 256
Greig, W. E. 1971, A&A, 10, 161
Gruenwald, R., & Viegas, S. M. 2000, ApJ, 543, 889
Harman, R. F., & Seaton, M. J. 1966, MNRAS, 132, 15
Henry, R. B. C., Liebert, J., & Boroson, T. A. 1989, ApJ, 339, 872
Herwig, F. 2000, A&A, 360, 952
Holtzman, J. A., Burrows, C. J., Casertano, S., Hester, J. J., Trauger, J. T., Watson, A. M., & Worthey, G. 1995, PASP, 107, 1065

Howarth, I. D. 1983, MNRAS, 203, 301
Jacoby, G. H., & Kaler, J. B. 1993, ApJ, 417, 209
Kaler, J., & Lutz, J. H. 1985, PASP, 97, 700
Kaler, J. B. 1983, ApJ, 271, 188
Kaler, J. B., & Jacoby, G. H. 1989, ApJ, 345, 871
———. 1990, ApJ, 362, 491
———. 1991, ApJ, 382, 134
Leitherer, C., et al. 2001, STIS Instrument Handbook, Version 5.1 (Baltimore: STScI)
Livio, M., & Soker, N. 1988, ApJ, 329, 764
———. 2002, ApJ, 571, L161
Manchado, A., Villaver, E., Stanghellini, L., & Guerrero, M. A. 2000, in ASP Conf. Ser. 199: Asymmetrical Planetary Nebulae II: From Origins to Microstructures, ed. J. H. Kastner, N. Soker, & S. Rappaport (San Francisco: ASP), 17
Meatheringham, S. J., & Dopita, M. A. 1991a, ApJS, 75, 407
———. 1991b, ApJS, 76, 1085
Meatheringham, S. J., Dopita, M. A., Ford, H. C., & Webster, B. L. 1988a, ApJ, 327, 651
Meatheringham, S. J., Dopita, M. A., & Morgan, D. H. 1988b, ApJ, 329, 166
Monk, D. J., Barlow, M. J., & Clegg, R. E. S. 1988, MNRAS, 234, 583
Pascoli, G. 1992, PASP, 104, 350
Peimbert, M. 1978, IAU Symp. 76, Planetary Nebulae, ed. Y. Terzian (Dordrecht: Reidel), 215
Peña, M., Peimbert, M., Torres-Peimbert, S., Ruiz, M. T., & Maza, J. 1995, ApJ, 441, 343
Rejkuba, M., Minniti, D., Gregg, M. D., Zijlstra, A. A., Alonso, M. V., & Goudfrooij, P. 2000, AJ, 120, 801

Rubin, R. H., et al. 2002, MNRAS, 334, 777
Savage, B. D., & Mathis, J. S. 1979, ARA&A, 17, 73
Schönberner, D. 1983, ApJ, 272, 708
Schönberner, D., & Tylenda, R. 1990, A&A, 234, 439
Shaw, R. A., & Kaler, J. B. 1989, ApJS, 69, 495
Shaw, R. A., Stanghellini, L., Mutchler, M., Balick, B., & Blades, J. C. 2001, ApJ, 548, 727 (Paper I)
Stanghellini, L., Corradi, R. L. M., & Schwarz, H. E. 1993, A&A, 279, 521
Stanghellini, L., Shaw, R. A., Mutchler, M., Palen, S., Balick, B., & Blades, J. C. 2002a, ApJ, 575, 178 (Paper II)
Stanghellini, L., Villaver, E., Manchado, A., & Guerrero, M. A. 2002b, ApJ, 576, 285
Stasinska, G., & Tylenda, R. 1986, A&A, 155, 137
Torres-Peimbert, S., & Peimbert, M. 1997, Planetary Nebulae, ed. H. Habing & H. Lamers (Dordrecht: Kluwer), 175
Umeda, H., Nomoto, K., Yamaoka, H., & Wanajo, S. 1999, ApJ, 513, 861
Vacca, W. D., Garmany, C. D., & Shull, J. M. 1996, ApJ, 460, 914
van der Marel, R. P., & Cioni, M. L. 2001, AJ, 122, 1807
Vassiliadis, E., Dopita, M. A., Morgan, D. H., & Bell, J. F. 1992, ApJS, 83, 87
Vassiliadis, E., & Wood, P. R. 1994, ApJS, 92, 125
Vassiliadis, E., et al. 1998, ApJ, 503, 253
Villaver, E., García-Segura, G., & Manchado, A. 2002a, ApJ, 571, 880
Villaver, E., Manchado, A., & García-Segura, G. 2002b, ApJ, 581, 1204
Weidemann, V. 1987, A&A, 188, 74
Zanstra, H. 1931, Publ. Dom. Astrophys. Obs. Victoria, 4, 209